Plasmonics (2025) 20:155–166
https://doi.org/10.1007/s11468-024-02264-x

RESEARCH

Advanced High-Performance Biochemical Sensor: Synchronous SPR Excitation with Parallel Multiple Single-Mode Fibers (SMFs)

Lin Yang[1] · Chao Liu[1] · Wei Liu[1] · Xili Lu[2] · Jingwei Lv[1] · Jianxin Wang[1] · Yan Lv[1] · Qiang Liu[1] · Paul K. Chu[3]

Received: 14 January 2024 / Accepted: 4 March 2024 / Published online: 19 March 2024

Abstract

This sensor utilizes conventional single-mode fiber (SMF) to create a refractive index (RI) surface plasmon resonance (SPR) system. To enhance its capabilities, multiple SMFs are employed in parallel, enabling the synchronous and collective activation of surface plasmon polaritons (SPPs) to achieve rapid responses for the detection of biochemical analytes in the infrared spectrum, ranging from 1200 to 6900 nm. The sensor's characteristics are meticulously analyzed using the all-vector finite element method (FEM). The sensing medium comprises gold, chosen for its exceptional corrosion resistance and stability. Gold facilitates the efficient release of free electrons, promoting the coupling effect between the first-order *x*-odd mode and SPP mode, which is particularly prominent in this setup. The investigated sensor showcases remarkable performance metrics, which boasts an impressive maximum wavelength sensitivity of 70,000 nm/RIU, accompanied by an average sensitivity of 14,204.55 nm/RIU and an exceptional resolution reaching 1.43×10^{-6} RIU. Notably, this splendid performance is consistent across a wide RI range, spanning from 1.00 to 1.44. Additionally, the signal-to-noise ratio (SNR) and figure of merit (FOM) are exceptional, while the walk-off length of 205 m far exceeds the transmission distance of microstructure optical fibers (MOFs). In comparison to similar MOFs, this SMF-based sensor offers distinct advantages. Its simple structure, cost-effectiveness, and exceptional performance address manufacturing challenges and overcome existing technical limitations. This breakthrough technology holds the potential to revolutionize various fields, including environmental monitoring, biomedicine, and chemical analysis.

Keywords Parallel sensing structure · Refractive index (RI) detection · Surface plasmon resonance (SPR) · Single-mode optical fiber (SMF) · Biochemical monitoring

Introduction

The increasing demand for biochemical research, food safety, medical diagnostics, and environmental monitoring is rendering accurate detection of analyte refractive indexes (RIs) important, and surface plasmon resonance (SPR) sensing technology has drawn much interest [1–4]. Essentially, SPR is an optical phenomenon involving resonant excitation of electromagnetic surface waves and collective oscillations of free electrons in metals [5, 6]. When the metal-medium interface is excited, the electromagnetic wave energy is absorbed and a narrower absorption peak can be obtained at the resonance wavelength (RW) [7, 8]. The process is sensitive to minute variations of the analyte RIs in the vicinity and can be exploited for sensing with high sensitivity and resolution [9]. Owing to advantages such as real-time label-free monitoring, transcendent output characteristics, high selectivity, and low detection, the technology has been applied to various biological, chemical, medical, and interdisciplinary fields [10–12].

During the SPR sensing, in order to solve the critical problems of interparticle momentum matching and platform miniaturization and to further expand the application space of this technology, the novel microstructure optical

✉ Chao Liu
msm-liu@126.com

[1] School of Physics and Electronic Engineering, Northeast Petroleum University, Daqing 163318, China

[2] School of Materials Science and Chemical Engineering, Harbin Engineering University, Harbin 150001, China

[3] Department of Physics, Department of Materials Science and Engineering, and Department of Biomedical Engineering, City University of Hong Kong, Tat Chee Avenue, Kowloon, Hong Kong, China

fiber (MOF) has created an "academic wave" in the research field with its outstanding features such as small size, flexible multi-parameter functionality, and endless single-mode operation as well as adjustable chromaticity dispersion [13–15]. As a result, a variety of MOF sensors based on SPR have sprung up. The peers have done a large number of transcendent research works, including high sensitivity (216,000 nm/RIU) [16], infrared region (1300–2400 nm) [17], low RIs (1.19–1.29) [18], high RIs (1.49–1.54) [19], and broad RIs (1.00–1.37) [20] for analyte detection. At the same time, our team has also produced many valuable research results that continue to contribute the rapid development of this field. For example, in 2017, a double-open-loop structure sensor was proposed which can operate in the mid-infrared range [21]. In 2018, a symmetrical dual-D sensor with mutual coupling was studied [22]. In 2021, the development process and bottlenecks to be broken in this field were summarized [23].

Even though MOFs have many unique advantages, it is undeniable that it is difficult to manufacture MOF and deposit high-quality nano-films onto the wall of air holes inside the MOF. In order to overcome this bottleneck, novel attempts may be devoted to traditional SMFs. The manufacturing technology of single-mode fiber (SMF) is particularly mature, low cost, easy to mass production, and more convenient for practical application [24, 25]. Since the 1970s, much efforts are focused on SPR sensors based on SMFs [26, 27]. For example, in 2014, Yadav et al. proposed a sensor for protein detection with a sensitivity of 1500 nm/RIU [28]. In 2021, Gong et al. designed a dual-channel sensor for DNA detection that conveys a sensitivity of 1899 nm/RIU [29]. Liu et al. studied a D-type sensor that can simultaneously detect refractive index and temperature, with a maximum sensitivity of 6300 nm/RIU [30].

The common problems in the above research are that the SPR sensor based on SMF has poor optical characteristics such as sensitivity and difficult mode coupling, which limits its further development. Taking all things into consideration, we present the SMF in parallel combination for the first time, which significantly improves the output properties and can be compared to the MOF. Herein, a "two-layer sandwiched" structure is designed. The SPR sensor consists of three single-mode optical fibers in parallel and two sets of gold films deposited on the polished inner surface for super-characteristic detection of analytes in the infrared range. The finite element method (FEM) is adopted in the analysis, and gold with excellent corrosion resistance and conductivity is chosen as the plasmonic nano-sensing material. In manufacturing the sensor, the plasmonic film is polished to shorten the distance between the plasmonic film and fiber core in order to facilitate energy transmission and improve the mode coupling efficiency. Compared to the conventional single D-type structure, synchronization and superposition of the excited SPR are accomplished on account of the special parallel structure as well as dual coupling mechanisms of self and mutual coupling. The proposed sensor shows an average sensitivity of 14,204.55 nm/RIU and a maximum sensitivity of 70,000 nm/RIU. It has a large RI detection range of 1.0–1.44, covering the RI of many common biochemical samples. Therefore, based on its excellent performance and simple structure, the sensor is expected to have large potential in biochemical sensing such as uric acid, pathogenic bacteria, and acetylcholine.

Model of Structural Optimization and Manufacturing Method

Figure 1(a) depicts the schematic structure of the SPR sensor composed of three polished SMFs in parallel. The SMF is a step-type fiber made of fused silica, and the RI of the fiber core is greater than that of the cladding. When light propagates in the fiber, most of the energy is restricted to the fiber core according to the principle of total internal reflection (TIR). In order to improve the mode coupling efficiency, the SMFs are polished to reduce the distance between the fiber core and gold film to facilitate transfer the light energy from the inner fiber core to the gold film surface to stimulate free electrons resulting in pronounced SPR effects.

In practice, the optical fiber wheel polishing machine is employed for the processing and preparation of D-type optical fibers [31]. The computerized intelligent platform precisely adjusts the spatial position of the grinding wheel, optimizing parameters such as grinding speed, downforce, and sandpaper particle fineness to achieve a uniform surface on the D-type optical fiber. Furthermore, magnetron sputtering is utilized as a physical vapor deposition technique for growing thin films on substrate surfaces [32]. Known for its superior film quality and precise control over process parameters, this method finds extensive use in producing nano-metal films. By fine-tuning magnetron sputtering parameters and optimizing the preparation process, high-quality gold films are achieved. Following the polishing and coating of the optical fiber, the combination of optical fiber fixing fixture, rotating platform, and spiral micrometer can precisely control the position and angle of optical fiber, facilitating effective and accurate optical fiber docking.

To optimize the structure, a model is created by transitioning from the single D-shape to double D-shape ones as shown in Fig. 1(b)–(d). Compared with the single D-shape structure, the double D-shape structure has both the self and mutual coupling mechanisms to increase the SPR effects. This multi-SMF parallel sensor is a "two-layer sandwiched" structure, and the advantage lies in synchronous excitation of SPR to produce multiple and superposition properties. It is noted that such a structure with multi-D-type parallel coupling

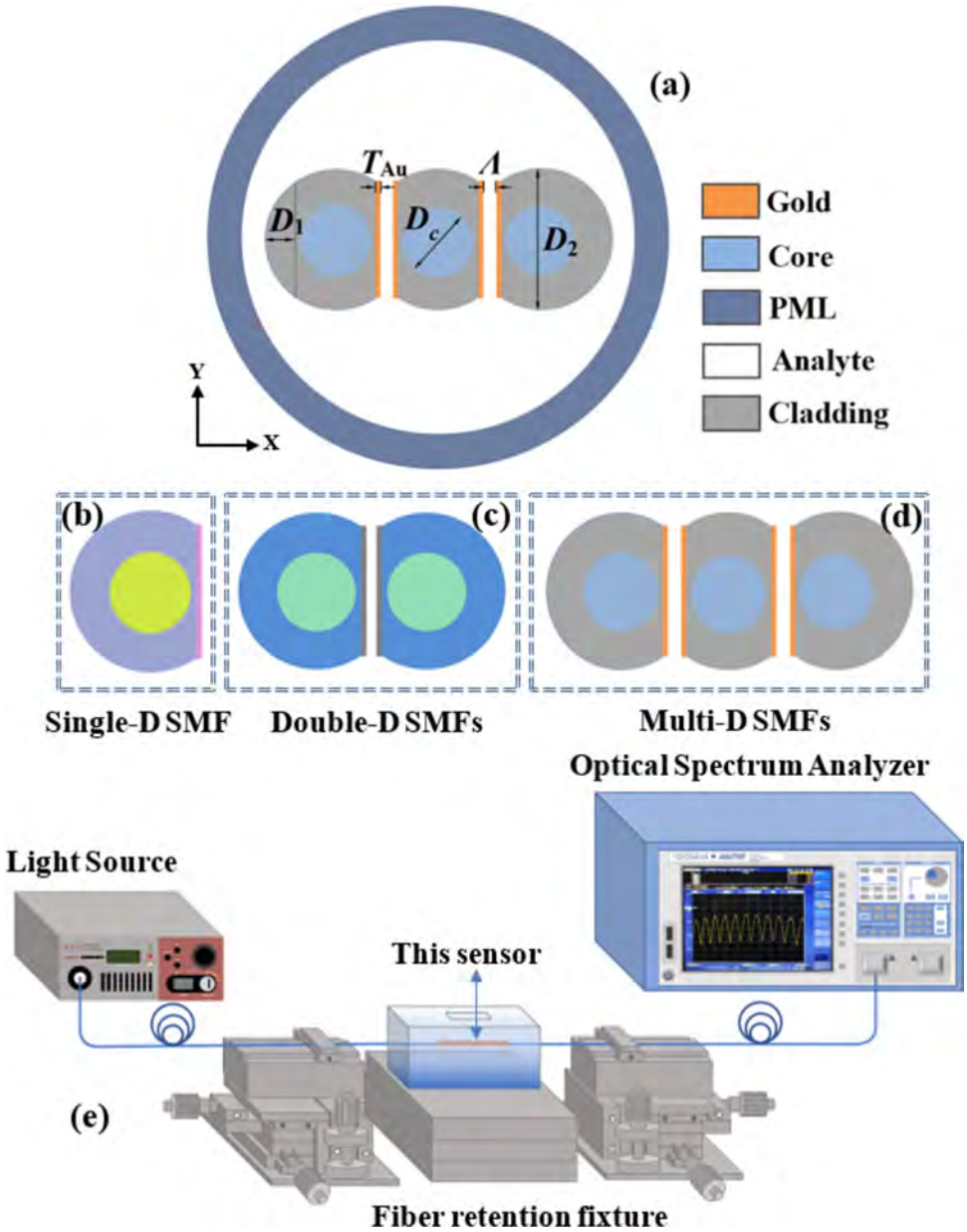

Fig. 1 **a** 2D cross-sectional depiction of the sensor. **b** Single D-shape SMF. **c** Double D-shape SMFs. **d** Multiple D-shape SMFs in parallel. **e** Simulation platform for bio-chemical sensing

has seldom been studied, and simulation results show that the performance of this sensor is better than that of the single and double D-type SMF sensors as shown in Fig. 1(b) and (c). By optimization, the core diameter (D_c) of 8.2 μm remains unchanged. The SMF diameter after corrosion (D_1) is 13 μm, SMF polishing depth (D_2) is 3 μm, SMF spacing (Λ) is 0.3 μm, and gold film thickness (T_{Au}) is 40 nm. In this case, the SMF spacing and gold film thickness shown in the structural schematic (Fig. 1) have been enlarged for ease of viewing and model harmonization. The Drude-Lorentz model is a classical model that can be used to calculate the dielectric constants of materials and for gold (Au); the dielectric constant can be calculated by Eq. (1) [33]:

$$\varepsilon(\omega) = \varepsilon_{\infty} - \frac{\omega_p^2}{\omega(\omega + i\omega_c)} \tag{1}$$

where $\varepsilon(\omega)$ is the complex frequency-dependent dielectric constant; $\varepsilon_{\infty} = 9.48$ is the high-frequency limit of the dielectric constant; ω is the angular frequency of the incident wave; $\omega_p = 1.36 \times 10^{16}$ rad/s is the angular frequency of the plasma, which is related to the electron density of the metal; and $\omega_c = 1.45 \times 10^{14}$ rad/s is the damping frequency related to the relaxation time of the electrons in the metal.

The RI of fused silica can be calculated by Sellmeier equation, which is an empirical formula that is suitable to the far infrared light and the relation between RI of

materials and the wavelength is determined by Eq. (2) [34–36]:

$$n^2 - 1 = \frac{B_1\lambda^2}{\lambda^2 - C_1} + \frac{B_2\lambda^2}{\lambda^2 - C_2} + \frac{B_3\lambda^2}{\lambda^2 - C_3} \quad (2)$$

where n stands for the RI of fused silica at a given wavelength λ in micrometers, and B_1, B_2, B_3, and C_1, C_2, C_3 are the Sellmeier coefficients for fused silica, which are experimentally determined constants ($B_1 = 0.696163$, $B_2 = 0.4079426$, $B_3 = 0.8974794$, $C_1 = 4.67914826 \times 10^{-3}$ μm^2, $C_2 = 1.35120631 \times 10^{-2}$ μm^2, and $C_3 = 97.9340025$ μm^2).

The COMSOL Multiphysics software was implemented to analyze the modal characteristics based on the full-vector finite element method (FEM) [37]. The circular perfect matching layer (C-PML) is adopted to reduce unnecessary electromagnetic reflection as the boundary absorption condition [38]. The optimal numerical solution is determined by grid division and mode calculation. The energy transfer during mode coupling can be described by confinement loss (CL) as shown by the following equation [6]:

$$\alpha_{\text{loss}}(\text{dB/cm}) = 8.686 \times \frac{2\pi}{\lambda}\text{Im}[n_{\text{eff}}] \times 10^4 \quad (3)$$

where λ denotes the operating wavelength in micrometers and Im[n_{eff}] is the imaginary part of the effective refractive index. CL occurs due to the energy coupling between the core-guided mode and SPP mode derived from the simulation results.

Figure 1(e) shows the platform for biochemical sensing. The multi-SMF parallel sensor is placed in the reaction chamber. The two ends of the sensor are fused with the SMF and light is emitted from the light source through the SMF to the sensor and finally to the optical spectrum analyzer (OSA). Because the SPR sensor is extremely sensitive to the variation of analyte RIs in the surroundings, the output spectrum red-shifts or blue-shifts when the RI changes, and by analyzing the resonance wavelength, the optical characteristics of the sensor can be assessed.

Mode Coupling Mechanism and Polarized State Analysis

Figure 2(a)–(g) presents the relationship with wavelength in mode coupling, and several typical electric field distributions are displayed to reveal the basic principle of SPR excitation from the perspective of phase matching. Typically, the dispersion and CL of the fiber are related to Re(n_{eff}) and Im(n_{eff}), respectively. Figure 2(a) shows that as the incident light wavelength goes up, the real parts of the core-guided mode and SPP mode decrease, whereas the CL in the fiber core increases initially and then decreases. At a wavelength of 2430 nm, the CL reaches the maximum and the real part curves of the two modes jump and then cross at random, indicative of the phase matching point of the two modes at this wavelength. The maximum CL reveals that more energy is transferred from the inner core to the surface of the gold film to stimulate free electrons and produce strong SPR effects. Figure 2(b)–(g) presents the electric field distributions of several typical modes. Figure 2(b) and (c) shows the electric field distributions of the core-guided mode and SPP mode without coupling, respectively. At this time, most of the energy only exists in the inner core and the surface of the metal film. Figure 2(d) describes the electric field distribution with energy coupling occurred between the two modes, and Fig. 2(e)–(g) shows the higher-order modes of the core-guided mode and SPP mode at a refractive index of 1.37. It is noted that the higher-order modes can probably interact with the plasmonic mode at higher wavelengths. However, the loss spectrum of the fundamental mode shows a single resonance peak, indicating that it is not affected by the other higher-order modes. In addition, the fundamental mode is commonly used to excite SPP mode due to their stronger coupling effect in previous literatures. Therefore, by considering the mode coupling effect and stability of the electric fields, the first-order mode is chosen in the subsequent study.

Figure 3 exhibits the columnar distributions of CL with wavelength for the core-guided mode (odd mode and even mode) in the x- and y-polarized states together with the

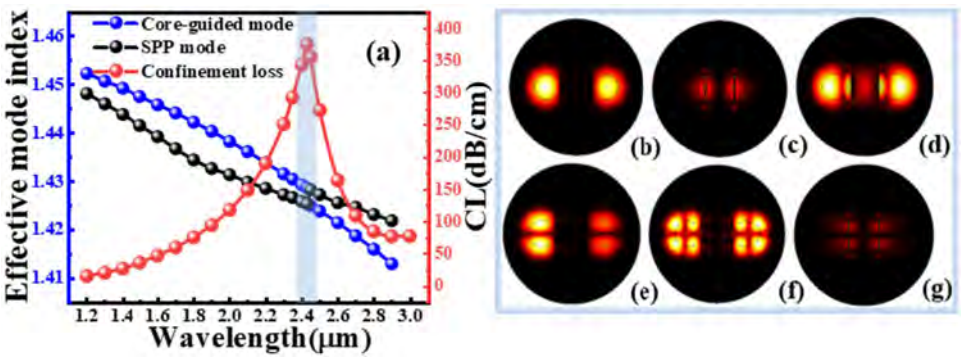

Fig. 2 **a** Mode coupling mechanism. **b–g** Electric field distributions of modes with different orders ($n_{\text{air}} = 1.0$, $n_a = 1.37$, $T_{\text{Au}} = 40$ nm, $\Lambda = 0.3$ μm, $D_1 = 3.0$ μm, and $D_2 = 13$ μm)

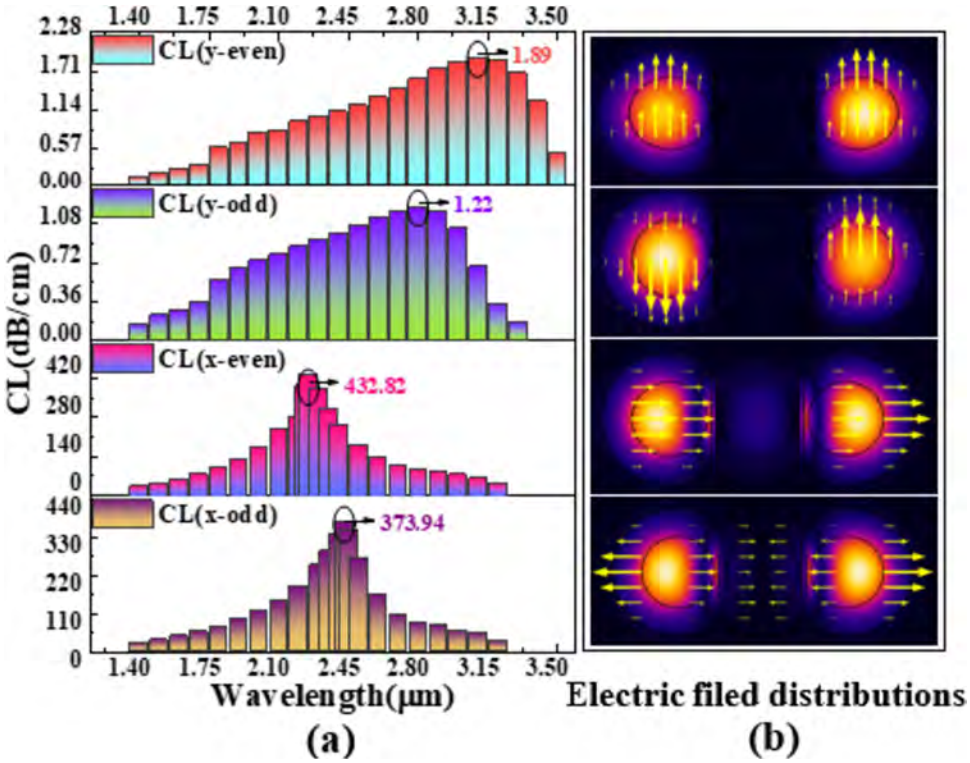

Fig. 3 Columnar and electric field distributions of different polarized states: *y*-even mode, *y*-odd mode, *x*-even mode, and *x*-odd mode ($n_{air}=1.0$, $n_a=1.37$, $T_{Au}=40$ nm, $\Lambda=0.3$ μm, $D_1=3.0$ μm, and $D_2=13$ μm)

electric field distributions at resonance. Since the SPR sensor is composed of multiple single-mode fibers in parallel, that is, a multi-core structure, both the odd and even modes exist when the light is transmitted in the fiber core. Therefore, the core-guided modes of each mode are energetically coupled to the SPP modes in spite of obvious differences. The CL curves in Fig. 3(a) shows that the CL of the core-guided mode in the *x*-polarized state is much larger than that in the *y*-polarized state, indicating that energy coupling of the core-guided mode and SPP mode in the *x*-polarized state is more significant. The electric field distributions in Fig. 3(b) reveal the coupling effects more clearly. For the odd mode and even mode in the *x*-polarized state, the CL peak of the *x*-even mode is slightly larger than that of the *x*-odd mode but the difference is small. By calculating the sensitivity of the output characteristics, the *x*-odd mode is superior and hence, the *x*-odd mode of the core-guided mode is employed in the following evaluation.

Comparison of Common Plasmonic Materials

It is critical to select the appropriate plasmonic materials in mode coupling to enhance the SPR effects. Here, common metal materials such as gold and silver are chosen and indium tin oxide (ITO) is examined due to the low cost and extended wavelength in the infrared region [39, 40]. Figure 4(a)–(g) displays the dependence of CL on the resonance wavelength (RW) and electric field distributions at resonance for the three plasmonic materials. With the analyte RIs change from 1.36 to 1.37, the CL curves corresponding to the coated gold and silver films show a blue-shift trend, while the CL curves corresponding to the coated ITO film show a red-shift

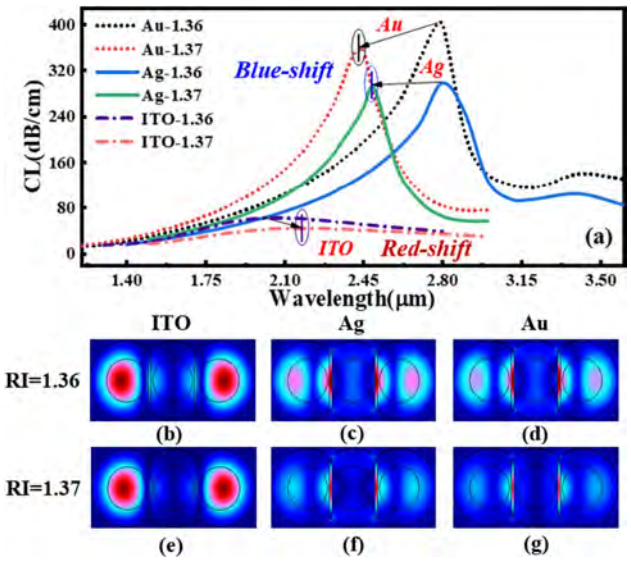

Fig. 4 Variation of CL depending on the wavelength of the fibers coated with Au, Ag, and indium tin oxide (ITO) for analyte RIs from 1.36 to 1.37 ($n_{air}=1.0$, $T_{Au}=40$ nm, $\Lambda=0.3$ μm, $D_1=3.0$ μm, and $D_2=13$ μm)

trend. In terms of the RW offset length, the gold film–coated sample has the largest offset (Au > Ag > ITO). Generally, the sensitivity is positively correlated with the wavelength offset, so the model presents the optimal sensitivity for the sample with the gold film. By observing the resonance peaks, the CL peak is higher and sharper when coated with gold film, further indicating that phase matching between the core-guided mode and SPP mode is better. In addition, when the analyte RI is 1.36, the electric field distributions in Fig. 4(b)–(d) show that gold as the plasmonic material results in more energy transferred from the fiber core to film surface. Hence, the electric field distribution in Fig. 4(d) is higher at the metal film and lower at the fiber core relative to Fig. 4(b) and (c). The results show that the two-mode coupling effect of the gold film is best for the same RI. With the analyte RIs increase from 1.36 to 1.37 for the gold and silver films, the two-mode coupling effects are enhanced but those of the ITO film weaken. The curves and light fields reflect this phenomenon. Together with the outstanding oxidation resistance and real-time and prolonged detection in aqueous solutions, gold is undoubtedly the best plasmonic medium.

Parameter and Structure Optimization

The structural parameters are derived by continuous adjustment and improvement of the model. Figure 5(a)–(m) shows the cross-sections of the SMF structure, parameter variation curves, and corresponding contour diagrams of the model for various parameters. The plasmonic sensor generates SPP waves through the metal layer, so that it is critical to optimize the film thickness. As aforementioned, gold is adopted due to the good stability, corrosion resistance, and electrical conductivity [41]. Figure 5(b) shows the dependence of the CL on the RW for different gold film thicknesses. When the thicknesses of the gold film (T_{Au}) increase from 30 to 60 nm, the CL peaks increase first and then decrease and the RW blue-shifts. For $T_{Au} = 40$ nm, the CL peak is the sharpest and the full-width at half-maximum (FWHM) is the narrowest, indicative of the most obvious SPR effects. The contour diagrams in Fig. 5(c) show the changing relationship and further analysis discloses that the thickness of the gold film alters the number of free electrons. A gold film that is too thick prevents photons inside the core from passing through the metal layer to stimulate free electrons to produce the SPR effects and the optimal T_{Au} is determined to be 40 nm.

The sensor is composed of multi-SMFs in parallel and exhibits both the self-coupling and mutual coupling mechanisms, so that the distance between the fibers plays a key role in mode coupling. Figure 5(e) presents the CL curves for different spacings (Λ). When the pitch is changed from 0.2 to 0.5 μm with an increment of 0.1 μm, the CL peak first increases and then decreases. Meanwhile, the FWHM decreases initially and then increases gradually. When the spacing is 0.3 μm, the CL peak is the largest, indicating the best coupling between the core-guided mode and SPP mode. Figure 5(f) reveals a blue-shift as the spacing is varied from 0.2 to 0.3 μm and there is a red-shift as the spacing is changed from 0.3 to 0.5 μm. When the spacing is 0.3 μm, the display on the right shows that it is reddish brown at the resonance wavelength, that is, maximum CL. This is consistent with Fig. 5(e), meaning that if the Λ is too small, coupling between the modes will be inhibited. If Λ is too large, the energy transmission efficiency decreases significantly during mode coupling and so the optimal Λ is 0.3 μm.

Figure 5(h) illustrates the correlation between CL and resonance wavelength for various polishing depths (D_1). Through multiple simulation calculations, the optimal range for the D_1 size has been determined to fall within the range of 2.6 to 3.2 μm, ensuring the optimal performance of the sensor design. To elaborate, if the polishing depth exceeds this range, there is a risk of compromising the internal structure of the fiber core, resulting in significant transmission loss and rendering the stimulation of SPR unattainable. Conversely, if the polishing depth is below this range, it fails to create the necessary evanescent wave leakage window, thereby impeding the efficient transfer of optical energy from the fiber core to the film surface.

Generally, the diameter of SMF is about 125 μm. When SMF is applied as the carrier of SPR sensor, appropriate corrosion of the fiber is conducive to coupling between the core-guided mode and SPP mode. At this time, more energy is transferred from the fiber core to metal surface and free electrons are excited to produce more intense SPR effects. In the modeling, SMF is etched and the diameter of the etched fiber (D_2) is controlled to be between 13 and 16 μm. Figure 5(k) and (l) shows the CL curve and contour diagram with wavelengths, respectively. Figure 5(k) shows that as D_2 is increased from 13 to 16 μm, the CL peak gradually decreases, the FWHM becomes narrower, and the resonance wavelength shifts to the long wavelength (red-shift). These changes are reflected in the contour diagram in Fig. 5(l). As D_2 increases, the RW changes from reddish brown to light red, but it is always in the red color system indicating that the CL does not fluctuate greatly. The red area in the contour diagram tilts to the right indicative of a red-shift and therefore, the optimal D_2 is 13 μm.

To sum up, the optimal structural parameters are $T_{Au} = 40$ nm, $\Lambda = 0.3$ μm, $D_1 = 3.0$ μm, and $D_2 = 13$ μm.

Sensing Properties

In order to evaluate properties of the proposed sensor, amplitude sensitivity is considered in this work. It can be expressed as

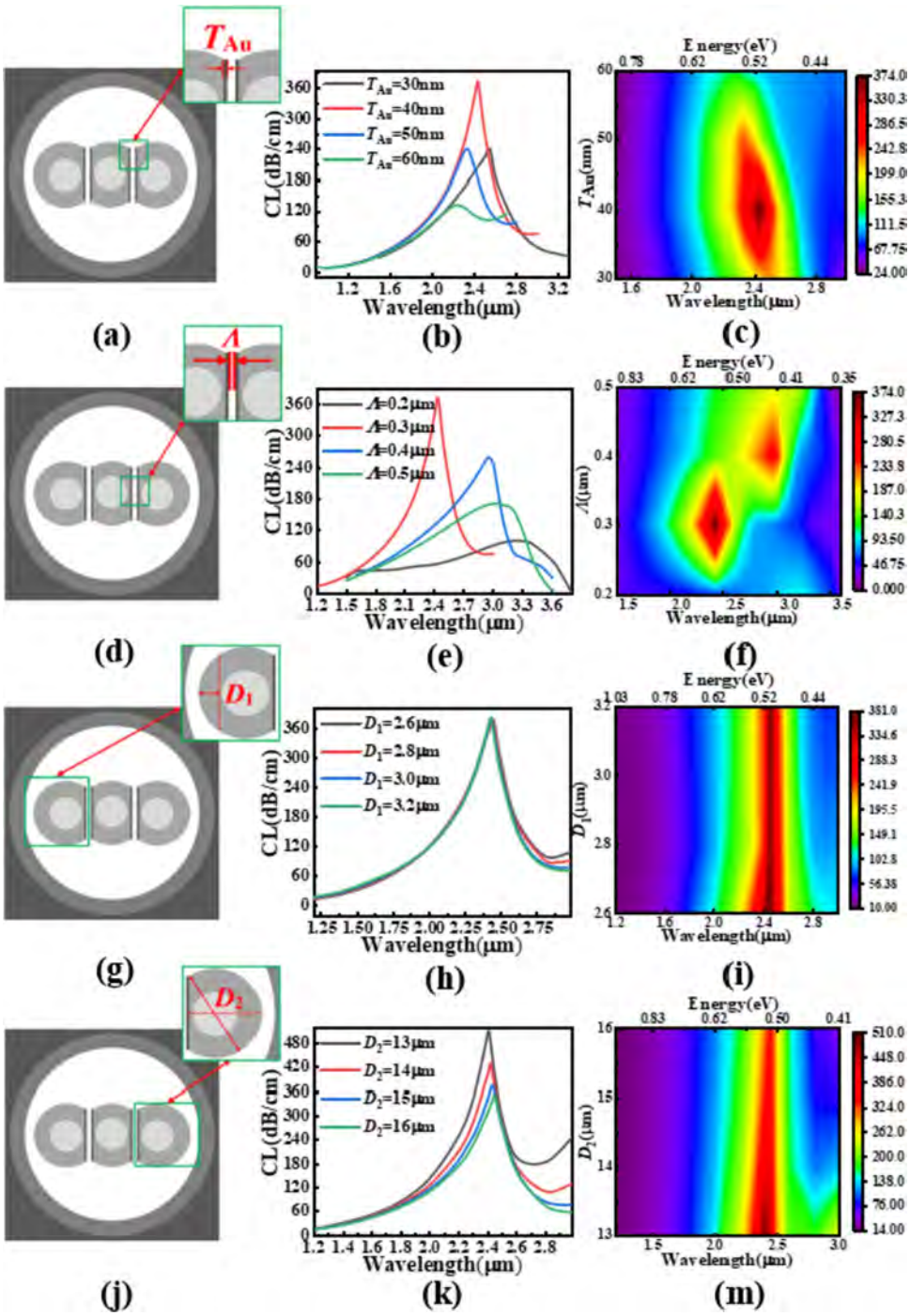

Fig. 5 **a**, **d**, **g**, **j** Cross-sections of the multi-SMF structure for diverse theoretical parameters: T_{Au}, Λ, D_1, and D_2. **b**, **e**, **h**, **k** Dependence of CL on wavelengths with T_{Au}, Λ, D_1, and D_2. **c**, **f**, **i**, **m** Parametric analysis with contour diagrams ($n_{air}=1.0$, $n_a=1.37$, $T_{Au}=40$ nm, $\Lambda=0.3$ μm, $D_1=3.0$ μm, and $D_2=13$ μm)

$$S_{am}=\frac{1}{\alpha(\lambda,n)}\frac{\partial\alpha(\lambda,n)}{\partial n}(\mathrm{RIU}^{-1}) \tag{4}$$

where $\alpha(\lambda, n)$ refers to the confinement loss $\alpha_{loss.}$ Figure 6 shows S_{am} of the proposed sensor with the refractive index ranging from 1.15 to 1.35. It can be seen that the amplitude sensitivity decreases gradually with increasing the refractive index. The amplitude sensitivity is simple to operate at a fixed wavelength, but the disadvantage is that the sensitivity is low. Therefore, spectral sensitivity is studied in this work, which is another important parameter to evaluate sensing performance.

The spectral sensitivity of the sensor is calculated by means of detecting the shift of resonance peaks for different refractive indexes of the analytes as shown by Eq. (5) [42]:

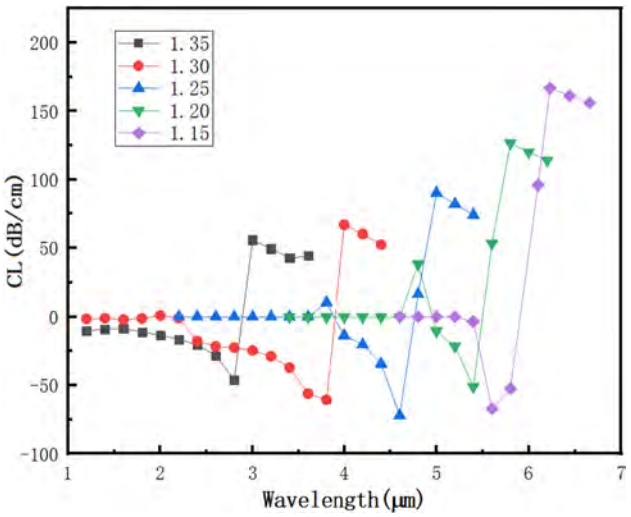

Fig. 6 Amplitude sensitivity of the sensor

$$S_W(nm/RIU) = \frac{\Delta\lambda_{peak}}{\Delta n_a} \tag{5}$$

where $\Delta n_a = 0.01$ refers to the variation of two successive analyte RIs and $\Delta\lambda_{peak}$ denotes the difference of the resonant peaks with analyte RI variation.

Figure 7(a)–(d) shows the dependence of CL on RW with analyte RIs from 1.00 to 1.44. As the analyte RIs increase gradually, the resonance peak decreases, FWHM increases, and RW ranges from 1200 to 6900 nm with a blue-shift. It is noted that such a long wavelength range needs a special light source [43]. The fundamental reason is that as the analyte RIs increase, Re(n_{eff}) of the SPP mode decreases, but Re(n_{eff}) of the core-guided mode is almost unchanged. Eventually, the phase matching point moves to a short wavelength. More specifically, in the range of 1.00–1.30, the FWHM does not change significantly. It is relatively narrow

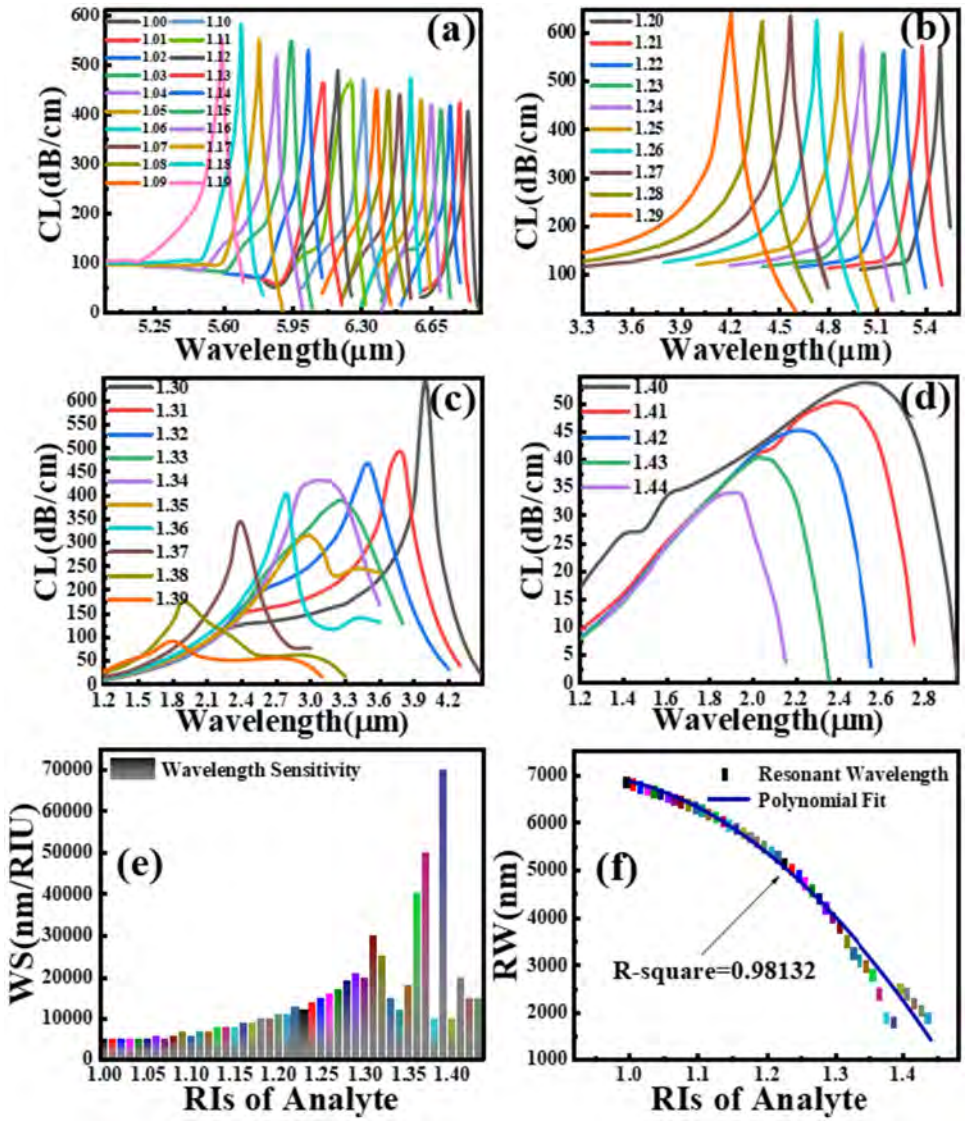

Fig. 7 Dependence of the wavelength sensitivity on wavelengths for different analyte RI ranges: **b** 1.00–1.19, **d** 1.20–1.29, **f** 1.30–1.39, and **h** 1.40–1.44. **e** Histograms showing wavelength sensitivity for different analyte RIs. **f** Polynomial fit of between RW and analyte RIs ($n_{air} = 1.0$, $T_{Au} = 40$ nm, $\Lambda = 0.3$ μm, $D_1 = 3.0$ μm and $D_2 = 13$ μm)

and the CL peak is sharper. In the range of 1.31–1.39, the FWHM is significantly different. With increasing analyte RIs, the CL peak decreases gradually and FWHM widens. In the range of 1.40–1.44, the FWHM is relatively wide but gradually narrows and CL is relatively small.

Figure 7(e) exhibits the relationship between wavelength sensitivity and analyte RIs. As the RIs increase, the wavelength sensitivity generally shows an upward trend but with only individual decrease, but the overall effect is not affected. The sensitivity is not regular because the sensor is more sensitive to samples with high refractive index; similar results have been found in Ref. [6, 18, 44]. The results reveal that maximum sensitivity of 70,000 nm/RIU and average sensitivity of 14,204.55 nm/RIU can be accomplished. It is worth mentioning that it is not common to obtain such a high average sensitivity in the ultra-wide RI detection range, indicating that the overall detection capability of this sensor is outstanding. This is further supported by the extraordinary resolution (R) characteristics in Eq. (6) [44]:

$$R(RIU) = \Delta n_a \frac{\Delta\lambda_{min}}{\Delta\lambda_{peak}} \tag{6}$$

where Δn_a represents the analyte RIs variation, $\Delta\lambda_{min}$ is the minimum wavelength resolution (0.1 nm), and $\Delta\lambda_{peak}$ stands for the shift of the CL peak in terms of the RW. Here, the best R is 1.43×10^{-6} RIU.

Figure 7(f) presents the polynomial fit to the RW for different analyte RIs revealing that the RW is negatively correlated with the analyte RIs. R-square and residual sum of squares are 0.98132 and 2.287, respectively, reflecting the ability to measure analytes accurately. The three prominent metrics for evaluating SPR sensors are the walk-off length, SNR, and FOM as shown by Eqs. (7)–(9) [45–48]:

$$L = \frac{\lambda}{n_{eff}^{even} - n_{eff}^{odd}}(m) \tag{7}$$

where n_{eff} (even) and n_{eff} (odd) are the effective RIs of the even and odd modes, respectively, and

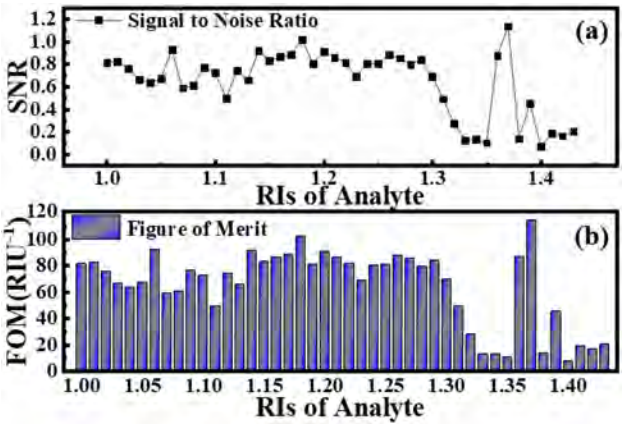

Fig. 8 Multi-SMF parallel sensor: **a** SNR and **b** FOM ($n_{\text{air}}=1.0$, $T_{\text{Au}}=40$ nm, $\Lambda=0.3$ μm, $D_1=3.0$ μm, and $D_2=13$ μm)

$$SNR = \frac{\Delta\lambda_{peak}}{FWHM} \tag{8}$$

$$FOM = \frac{S_w}{FWHM} \tag{9}$$

where FWHM means full-width at half-maximum. The higher the SNR of the sensor, the less noise is generated and the better the quality of the transmitted information. Meanwhile, a high FOM indicates a better detection limit.

Table 1 lists the walk-off lengths for different RIs in the x-polarized state. Compared with the SPR sensor based on MOF described previously, this multi-SMF parallel SPR sensor has a longer transmission distance and has better properties in practical detection. Figure 8(a) and (b) describes the distribution and trend of SNR and FOM, respectively. The optimal SNR is 1.13 and the best FOM is 113.19 RIU^{-1}.

Up to now, the most promising SPR sensor is the fiber type which has significant advantages such as miniaturization, low cost, real-time detection, and long-distance transmission. Typical fiber SPR sensors are based on SMF and MOF as summarized in Table 2 which reveals that this

Table 1 Walk-off lengths for different analyte refractive indexes

Analyte RIs	Re(n_{eff}) even mode	Re(n_{eff}) odd mode	Walk-off length (m)	Analyte RIs	Re(n_{eff}) even mode	Re(n_{eff}) odd mode	Walk-off length (m)
1.00	1.055558675	1.048270921	0.411649425	**1.37**	1.429122084	1.426906901	1.354290035
1.05	1.109492241	1.108430654	2.825957663	**1.38**	1.440652277	1.438879846	1.692590834
1.10	1.160776589	1.159718618	2.835618246	**1.39**	1.441418277	1.441044863	8.033984291
1.15	1.212074303	1.211288208	3.816332967	**1.40**	1.425524125	1.425506572	170.913757
1.20	1.263595503	1.259012807	0.65463646	**1.41**	1.428365911	1.428350253	191.5998086
1.25	1.315491736	1.31184288	0.822175569	**1.42**	1.433395146	1.43337959	192.8460815
1.30	1.369125388	1.367220154	1.574609946	**1.43**	1.436940922	1.436955557	204.9912858
1.35	1.409776285	1.409840768	46.57252479	**1.44**	1.440453986	1.440415668	78.29352947

Table 2 Comparison of sensing properties with the reported SPR-fiber sensors

Ref.	Characteristics	Det. Range	S_w (nm/RIU)	R (RIU)	Str. Diagram
[49]	H-shaped SMF-SPR sensor	1.33-1.39	7540	1.30×10^{-5}	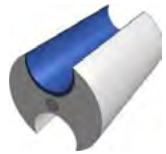
[50]	Microfluidic channel SMF-SPR sensor	1.33-1.35	13700	7.30×10^{-6}	
[51]	D-shaped honeycomb MOF-SPR sensor	1.33-1.39	14700	6.80×10^{-6}	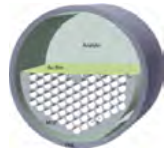
[52]	Composite material modified MOF-SPR sensor	1.33-1.37	4649.8	2.15×10^{-5}	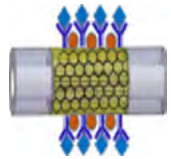
This work	Parallel Multi-SMFs SPR sensor	1.00-1.44	70000	1.43×10^{-6}	

supercharacteristic multi-SMF parallel sensor has outstanding features. Not only does it overcome some of the problems and challenges related to production but also fosters widespread application of SPR sensors.

Conclusion

A high-performance multi-SMF parallel sensor with synchronous SPR excitation is designed and investigated. Some of the problems associated with manufacturing of MOF sensors are solved. The finite element method (FEM) is employed in the analysis which discloses that the coupling efficiency between the modes can be enhanced by optimizing the structural parameters such as the fiber diameter after corrosion, fiber polishing depth, sensor spacing, and plasmonic film thickness. The sensor achieves fast response to analytes with optimal sensitivity, average sensitivity, and maximum resolution of 70,000 nm/RIU, 14,204.55 nm/RIU, and 1.43×10^{-6} RIU, respectively. This sensor realizes the possibility of simultaneous detection of gases and liquids in a larger range and broadens the transmission interval of infrared light (1200–6900 nm).

Author Contribution Yang Lin: conceptualization, methodology, software, and writing original draft. Chao Liu: conceptualization, data curation, writing review, and editing. Wei Liu: investigation. Xili Lu: conceptualization. Jingwei Lv: formal analysis. Jianxin Wang: funding acquisition and validation. Yan Lv: methodology, supervision, and formal analysis. Qiang Liu: validation. Paul K. Chu: project administration. All authors reviewed the manuscript.

Funding This work was jointly supported by Heilongjiang Provincial Natural Science Foundation of China (JQ2023F001), Outstanding young and middle-aged research and innovation team of Northeast Petroleum University (KYCXTD201801), Local Universities Reformation and Development Personnel Training Supporting Project from Central Authorities, Postdoctoral Scientific Research Development Fund of Heilongjiang Province (LBH-Q20081), City University of Hong Kong Donation Research Grant (DON-RMG No. 9229021), City University of Hong Kong Strategic Research Grant (SRG 7005505), and City University of Hong Kong Donation Grant (9220061).

Data Availability No datasets were generated or analyzed during the current study.

Code Availability Not applicable.

Declarations

Ethics Approval No ethical approval is required.

Consent to Participate Informed consent was obtained from all individual participants included in the study.

Consent for Publication Approved.

Competing Interests The authors declare no conflicts of interest.

References

1. Shakya A, Ramola A, Singh S, Van V (2022) Design of ultra-sensitive bimetallic anisotropic PCF SPR biosensor for liquid analytes sensing. Opt Express 30(6):9233–9255
2. Shakya AK, Singh S (2020) Design of biochemical biosensor based on transmission, absorbance and refractive index. Biosens Bioelectron: X 10:100089
3. Jain S, Choudhary K, Kumar S (2022) Photonic crystal fiber-based SPR sensor for broad range of refractive index sensing applications. Opt Fiber Technol 73:103030
4. Shakya AK, Singh S (2022) Design of novel Penta core PCF SPR RI sensor based on fusion of IMD and EMD techniques for analysis of water and transformer oil. Meas 188:110513
5. Pandey PS, Raghuwanshi SK, Kumar S (2021) Recent advances in two-dimensional materials-based Kretschmann configuration for SPR sensors: a review. IEEE Sens J 22(2):1069–1080
6. Singh S, Prajapati YK (2019) Highly sensitive refractive index sensor based on D-shaped PCF with gold-graphene layers on the polished surface. Appl Phys A 125:437
7. Haider F, Aoni RA, Ahmed R, Miroshnichenko AE (2018) Highly amplitude sensitive photonic crystal fiber based plasmonic sensor. J Opt Soc Am B 35(11):2816–2821
8. Liu C, Wang JW, Wang FM, Su WQ, Yang L, Lv JW, Fu GL, Li XL, Liu Q, Sun T, Chu PK (2020) Surface plasmon resonance (SPR) infrared sensor based on D-shape photonic crystal fibers with ITO coatings. Opt Commun 464:125496
9. Rifat AA, Haider F, Ahmed R, Mahdiraji GA, Adikan FRM, Miroshnichenko AE (2018) Highly sensitive selectively coated photonic crystal fiber-based plasmonic sensor. Opt Letters 43(4):891–894
10. Falah AAS, Wong WR, Adikan FRM (2022) Single-mode eccentric-core D-shaped photonic crystal fiber surface plasmon resonance sensor. Opt Laser Technol 145:107474
11. Liu W, Shi Y, Yi Z, Liu C, Wang FM, Li XL, Lv JW, Yang L, Chu PK (2021) Surface plasmon resonance chemical sensor composed of a microstructured optical fiber for the detection of an ultra-wide refractive index range and gas-liquid pollutants. Opt Express 29(25):40734–40747
12. Han HX, Hou DL, Zhao L, Luan NN, Song L, Liu ZH, Lian YD, Liu JF, Hu YS (2020) A large detection-range plasmonic sensor based on an h-shaped photonic crystal fiber. Sensors 20(4):1009–1016
13. Santos DF, Guerreiro A, Baptista JM (2017) SPR optimization using metamaterials in a D-type PCF refractive index sensor. Opt Fiber Technol 33:83–88
14. Liu W, Hu CJ, Zhou L, Yi Z, Shi Y, Liu C, Lv JW, Yang L (2022) A highly sensitive D-type photonic crystal fiber infrared sensor with indium tin oxide based on surface plasmon resonance. Mod Phys Lett B 36(1):2150499
15. Liu W, Liu C, Wang JX, Lv JW, Lv Y, Yang L, An N, Yi Z, Liu Q, Hu CJ, Chu PK (2023) Surface plasmon resonance sensor composed of microstructured optical fibers for monitoring of external and internal environments in biological and environmental sensing. Results Phys 47:106365
16. Haque E, Noman AA, Hossain MA, Hai NH, Namihira Y, Ahmed F (2021) Highly sensitive D-shaped plasmonic refractive index sensor for a broad range of refractive index detection. IEEE Photonics J 13(1):4800211
17. Wang YJ, Dong JL, Luo YH, Tang JY, Lu HH, Yu JH, Guan HY, Zhang J, Chen Z (2017) Indium tin oxide coated two-mode fiber for enhanced SPR sensor in near-infrared region. IEEE Photonics J 9(6):1–9
18. Yang Z, Xia L, Li C, Chen X, Liu DM (2019) A surface plasmon resonance sensor based on concave-shaped photonic crystal fiber for low refractive index detection. Opt Commun 430:195–203

19. De M, Markides C, Singh VK, Themistos C, Rahman BMA (2020) Analysis of a single solid core flat fiber plasmonic refractive index sensor. Plasmonics 15:1429–1437
20. Haque E, Hossain MA, Pham T, Namihira Y, Hai NH, Ahmed F (2019) Surface plasmonic resonance sensor for wider range of low refractive index detection. 2019 26th International Conference on Telecommunications (ICT). IEEE 479–484
21. Liu C, Lin Y, Lu XL, Liu Q, Wang FM, Lv JW, Sun T, Mu HW, Chu PK (2017) Mid-infrared surface plasmon resonance sensor based on photonic crystal fibers. Opt Express 25(13):14227–14237
22. Liu C, Su WQ, Liu Q, Lu XL, Wang FM, Sun T, Chu PK (2018) Symmetrical dual D-shape photonic crystal fibers for surface plasmon resonance sensing. Opt Express 26(7):9039–9049
23. Liu C, Lv JW, Liu W, Wang FM, Chu PK (2021) Overview of refractive index sensors comprising photonic crystal fibers based on the surface plasmon resonance effect [Invited]. Chin Opt Lett 19(10):102202
24. Liu W, Hu CJ, Zhou L, Yi Z, Liu C, Lv JW, Yang L, Chu PK (2022) A square-lattice D-shaped photonic crystal fiber sensor based on SPR to detect analytes with large refractive indexes. Phys E 138:115106
25. Yang T, He XL, Zhou X, Lei ZY, Wang YL, Yang J, Cai D, Chen SL, Wang XD (2018) Surface plasmon cavities on optical fiber end-facets for biomolecule and ultrasound detection. Opt Laser Technol 101:468–478
26. Slavik R, Homola J, Ctyroky J (1999) Single-mode optical fiber surface plasmon resonance sensor. Sens Actuator B 54:74–79
27. Otto A (1968) Excitation of nonradiative surface plasma waves in silver by the method of frustrated total reflection. Z Phys 216(4):398–410
28. Yadav TK, Narayanaswamy R, Bakar MHA, Kamil YM, Mahdi MA (2014) Single mode tapered fiber-optic interferometer based refractive index sensor and its application to protein sensing. Opt Express 22(19):22802–22807
29. Gong PQ, Wang YM, Zhou X, Wang SK, Zhang YN, Zhao Y, Nguyen LV, Ebendorff-Heidepriem H, Peng L, Warren-Smith SC, Li XG (2021) In situ temperature-compensated DNA hybridization detection using a dual-channel optical fiber sensor. Anal Chem 93(30):10561–10567
30. Liu L, Liu ZH, Zhang Y, Liu ST (2021) Side-polished D-type fiber SPR sensor for RI sensing with temperature compensation. IEEE Sensors J 21(15):16621–16628
31. Li MQ, Bai ZY, Zhang F, Hou MX, Wang Y, Liao CR, Jin W, Wang YP (2017) Red shift of side-polished fiber surface plasmon resonance sensors with silver coating and inhibition by gold plating. IEEE Photonics J 9(3):7103913
32. Koba M, Radosaw R, Firek P, Śmietanaa M (2015) Sensing properties of periodic stack of nano-films deposited with various vapor-based techniques on optical fiber end-face. Proceedings of SPIE - The International Society for Optical Engineering, 9655
33. Liu H, Wang M, Wang Q, Li HW, Ding Y, Zhu CH (2018) Simultaneous measurement of hydrogen and methane based on PCF-SPR structure with compound film-coated side-holes. Opt Fiber Technol 45:1–7
34. Shafkat A (2020) Analysis of a gold coated plasmonic sensor based on a duplex core photonic crystal fiber. Sens Bio-Sens Res 28:100324
35. Malitson IH (1965) Interspecimen comparison of the refractive index of fused silica. J Opt Soc Am 55:1205–1208
36. Tan CZ (1998) Determination of refractive index of silica glass for infrared wavelengths by IR spectroscopy. J Non-Cryst Solids 223:158–163
37. Liu W, Hu CJ, Zhou L, Yi Z, Liu C, Lv JW, Yang L, Chu PK (2020) Ultra-sensitive hexagonal PCF-SPR sensor with a broad detection range. J Mod Opt 67(20):1545–1554
38. Momota MR, Hasan MdR (2018) Hollow-core silver coated photonic crystal fiber plasmonic sensor. Opt Mater 76:287–294
39. Dash JN, Das R (2018) SPR based magnetic-field sensing in microchannelled PCF: a numerical approach. J Optics 20(11):1–11
40. Maria JP, Losego M, Leonard DN, Laughlin B, Duscher G (2006) Surface plasmon resonance in conducting metal oxides. J Appl Phys 100(5):054905
41. Wang JW, Liu C, Wang FM, Su WQ, Yang L, Lv JW, Fu GL, Li XL, Liu Q, Sun T, Chu PK (2020) Surface plasmon resonance sensor based on coupling effects of dual photonic crystal fibers for low refractive indexes detection. Results Phys 18:103240
42. Rifat AA, Mahdiraji GA, Sua YM et al (2016) Highly sensitive multi-core flat fiber surface plasmon resonance refractive index sensor. Opt Express 24(3):2485–2495
43. Zangooie S, Persson POA, Hilfiker JN, Hultman L, Arwin H (2000) Microstructural and infrared optical properties of electrochemically etched highly doped 4H–SiC. J Appl Phys 87:8497–8503
44. Gao D, Guan C, Wen Y, Zhong X, Yuan L (2014) Multi-hole fiber based surface plasmon resonance sensor operated at near-infrared wavelengths. Opt Commun 313:94–97
45. Liu C, Fu HH, Hu CJ, Zhou L, Shi Y, Lv JW, Yang L, Chu PK (2021) Optimization of photonic crystal fibers for transmission of orbital angular momentum modes. Opt Quant Electron 53:639
46. Mahfuz MA, Hossain MdA, Haque E, Hai NH, Namihira Y (2020) Dual-core photonic crystal fiber-based plasmonic RI sensor in the visible to near-IR operating band. IEEE Sensors J 20(14):7692–7700
47. Melwin G, Senthilnathan K (2020) High sensitive D-shaped photonic crystal fiber sensor with V-groove analyte channel. Optik 213:164779
48. Gandhi MSA, Senthilnathan K, Babu PR, Li Q (2019) Visible to near infrared highly sensitive microbiosensor based on surface plasmon polariton with external sensing approach. Results Phys 15:102590
49. Gomez-Cardona N, Reyes-Vera E, Torres P (2020) High sensitivity refractive index sensor based on the excitation of long-range surface plasmon polaritons in H-shaped optical fiber. Sensors 20(7):2111
50. Pathak AK, Viphavakit C, Rahman BMA, Singh VK (2021) A highly sensitive SPR refractive index sensor based on microfluidic channel assisted with graphene-Ag composite nanowire. IEEE Photonics J 13(2):6801008
51. Chen X, Bu WY, Wu ZF, Zhang HJ, Shum PP, Shao XG, Pu JX (2021) Near-infrared long-range surface plasmon resonance in a D-shaped honeycomb microstructured optical fiber coated with Au film. Opt Express 29(11):16455–16468
52. Wang Q, Wang BT (2018) Sensitivity enhanced SPR immunosensor based on graphene oxide and SPA co-modified photonic crystal fiber. Opt Laser Technol 107:210–215